Springer

KSME

Journal of Mechanical Science and Technology 24 (2) (2010) 609~618
www.springerlink.com/content/1738-494x
DOI 10.1007/s12206-009-1214-6

# Design optimization of a loop heat pipe to cool a lithium ion battery onboard a military aircraft †

YongJin Park, Sangook Jun, Sanghun Kim, and Dong-Ho Lee*

*Department of Mechanical & Aerospace Engineering, Seoul National University and Institute of Advanced Aerospace Technology, Seoul National University, Seoul, 151-742, Korea*

(Manuscript Received July 7, 2009; Revised August 17, 2009; Accepted September 30, 2009)

**Abstract**

The present paper proposes optimization procedures for loop heat pipe (LHP) designed to cool the lithium-ion battery for airborne high energy electric lasers (HEL) without power consumption. The LHP is more efficient than the air cooling device using bleed air. The battery temperature rising enlarges the permanent loss of its capacity and makes it unusable and unsafe. Cold speedy air around a flying aircraft becomes a good heat sink for dissipating the battery heat. The design objective is to reduce the weight of the LHP, considering the range of battery operating temperature and operational reliability. For numerical analysis, the total system of the LHP is analyzed through a thermohydraulic model and the heat transfer of the porous wick is predicted by the thin liquid film model. The thermal characteristics of the groove section are found by an analytical solution and a finite difference method. The design optimization is executed by using approximation models for the cases of (1) a fixed heat load, (2) a varied heat load without uncertainty consideration, and (3) a varied heat load with uncertainty consideration about the generated heat of the battery. As result of the optimization process, the weight of the LHP was reduced significantly. The optimized LHP for the varied heat load with uncertainty consideration case is most reliable and robust with slight increase of the weight.

*Keywords*: Loop heat pipe; Reliability based design optimization; Lithium ion battery; Airborne high energy laser system

## 1. Introduction

Loop heat pipes (LHP) are used to cool electric devices in a satellite. Their performance has been proven through many experiments and actual applications in satellites, electronic devices and aircrafts. Although the LHP has been studied by many researchers, published results about its optimum design were few.

Optimization of the LHP/ CPL (capillary pumped loop) has a very short history. For example, Vlassov [1] optimized the space based LHP with a cylindrical evaporator and an integral reservoir by using the deterministic optimization method to reduce the total mass of the LHP. His optimization results did not reflect the porosity and vapor groove section size in detail and were obtained based on a specific (fixed) heat load. Park [2] used approximation model, gradient based optimization tools and the weighting sum method to reduce the LHP mass and the its temperature.

A mathematical model for calculating the total performance of the LHP in steady state was developed in the late 1990's by Kaya, et Al. [3]. However, the mathematical model simplifies the thermal analysis of the evaporator, so it is difficult to predict actually the effects of the porosity, the particle diameter and groove size on the thermal performance of the LHP.

In this paper, to overcome this weakness of the model, a heat transfer analysis of the thin liquid film and the groove section was carried out. The thin liquid film model explains the evaporation phenomenon from a meniscus in the porous wick. The thin film flow at the evaporating extended meniscus is dominant in the enhancement of the evaporation heat transfer [4] and is driven by capillarity and disjoining pressure gradient. In this paper, the numerical thermal analysis of the porous wick is based on the Zhao et al. thin liquid film model [5]. The heat transfer analysis of the groove section to determine the size of the fin is based on Cao's analytical solution [6] and the conduction equation. To solve the conduction problem, a finite difference method (FDM) is applied.

Moreover, the capillary, boiling, and sonic limits of the LHP are considered for operational reliability.

A lithium-ion battery recently developed as the Saft VL8V has high power density of 6kW/kg for 15 second pulses [7]. The lithium ion battery dissipates the heat at about 2.2W per

† This paper was recommended for publication in revised form by Associate Editor Do Hyung Lee

*Corresponding author. Tel.: +82 2 880 7399, Fax.: +82 2 882 7927
E-mail address: donghlee@snu.ac.kr

one cell (Ex: SONY18650, 18D-65mm L, 39.4g) at 2C discharge rate [8]. And the permanent capacity loss is minimized when the battery temperature is kept lower than 10℃ [9]. The high restored energy and energy efficiency of the battery are maintained at the temperature of 10-20℃ [10]. If the battery is used as a momentary high energy dissipation device such as the HEL, it is important to cool it, because of the large heat generation of the battery and the consecutive unfavorable responses.

Because the HEL operates at altitudes of 10-30kft, the heat can be dissipated through the cold air near the airplane. The absolute temperature gradient across the components of the HEL should be less than 2K and the operating temperature should not exceed specific value [7]. The LHP is more efficient than the air blowing device linked to the air conditioning system [11]. Therefore, it is essential to cool the batteries near the laser system using the cold outer air and the LHP.

The optimization is performed by deterministic and reliability based methods to reduce mass of the LHP. The desired temperature is set to be near 10℃ to reduce the capacity loss and maintain the efficiency of the battery. The reliability based method considers the uncertainty related to the heat generation of the battery.

Because the discharge rate of the battery is varied according to mission requirement and the discharge rate is related to the heat generation, this varied heat load of the battery is considered in the optimization.

## 2. Numerical analysis

### *2.1 Thermohydraulic model of LHP*

The LHP consists of the evaporator, the compensation chamber, the vapor/liquid line, the condenser, etc. as shown in Fig.1. Assumptions and mathematical models refer to Adoni [12]. For energy balance, the energy relation is expressed as Eq. (1).

$$Q_{load} = Q_{v.l} + Q_{l.l} + Q_{cond} + Q_{e-amb} + Q_{c.c-amb} + Q_{loss} \tag{1}$$

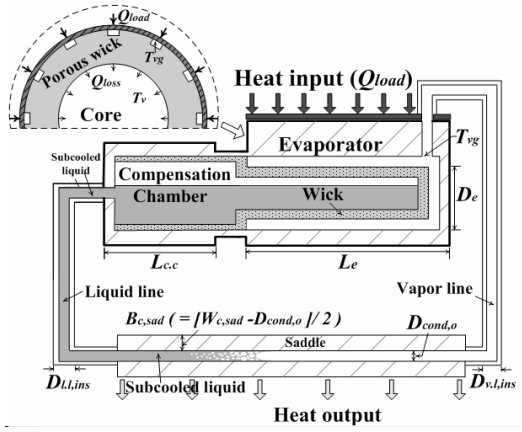


Fig. 1. Loop heat pipe schematic (not to scale).

In Eq. (1), $Q_{e-amb}$ is the heat transferred by natural convection from the evaporator to the ambient. The energy balance relation in the evaporator core and the compensation chamber is given by Eq. (2).

$$Q_{loss} + Q_{e-c.c} + x_{l.l}\, \dot{m} h_{fg} = U_{c.c-amb}\,(T_{c.c} - T_{amb})\, L_{c.c} + \dot{m}\, C_{p\_core}\,(T_{core} - T_{l.l}) \tag{2}$$

$Q_{loss}$ is a heat loss which is consumed to warm up the liquid in the compensation chamber and $Q_{e-c.c}$ indicates the heat exchanged between the evaporator and the compensation chamber by thermal conduction.

In the vapor and liquid line, the convective heat transfer coefficient of single phase flow depends on the working fluid temperature. Accordingly, to determine the coefficient, the average wall surface temperature is assumed and then updated until the calculated mean wall temperature is equal to the assumed average wall temperature.

For computation of the condenser heat transfer, the heat transfer coefficient of the radiator outer surface which is attached to the side skin of the flying aircraft is calculated by using the Eckert correlation [13] as follows:

$$H_{\infty} = 0.037\left[\frac{k_{\infty}}{z_c}\right]\mathrm{Pr}^{1/3}\left[\frac{\rho V z_c}{\mu}\right]^{4/5} \tag{3}$$

The characteristic length ( $z_c$ ) is the distance from the aircraft nose to the mid-position of the radiator. And the specific thermal conductance of the condenser and the saddle is given by Eq. (4).

$$\frac{1}{U_{cond}} = \frac{1}{2\pi k_{cond,t}}\ln\left(\frac{D_{cond,o}}{D_{cond,i}}\right) + \frac{1}{(D_{cond,o} + 2\eta_{sad}\, B_{c,sad})H_{\infty}} + \frac{\delta_{c,sad}}{k_{sad}\,(D_{cond,o} + 2\eta_{sad}\, B_{c,sad})} + \frac{1}{\pi D_{cond,i}\, H_{cond,i}} \tag{4}$$

$\eta_{sad}$ is the fin efficiency, explained in Eq. (8). $H_{cond,i}$ is the condensation heat transfer coefficient calculated by Thome's correlation [14]. A two phase pressure drop refers to Friedel's correlation [15]. The quality and the pressure gradient of the condensation are given by Eq. (5)-(6). The ODEs are solved by the 4th order Runge-Kutta method. $\alpha_v$ is the void fraction.

$$\frac{d\, x_{cond}}{d\, z} = -\frac{U_{cond}\,(T_{fg} - T_{sink})}{\dot{m}\, h_{fg}} \tag{5}$$

$$\frac{dP_{cond}}{d\, z} = -\phi_{lo}^2 \frac{f G^2}{2\rho_{lo} D_{cond,i}} - G^2 \frac{d}{dz}\left\{\frac{(1-x_{cond})^2}{\rho_l(1-\alpha_v)} + \frac{x_{cond}^2}{\rho_v \alpha_v}\right\} \tag{6}$$

The procedure for the thermohydraulic analysis is explained in detail in Fig. 2.

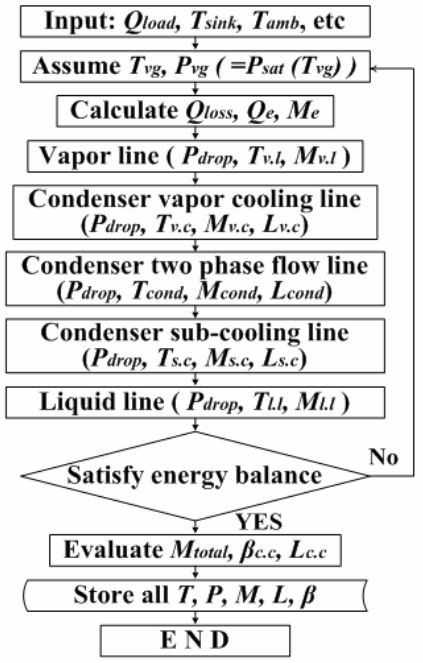


Fig. 2. Computation algorithm for the thermohydraulic analysis.

After computing the vapor groove temperature with the thermodydraulic model, the temperature of the evaporator inner wall is calculated by using the reported evaporative heat transfer coefficient [16].

The compensation chamber volume is determined by setting an appropriate liquid volume fraction. The fluid inventory condition derives the following relation for the cold case [17].

$$V_{c.c} = \frac{M_{c.c}}{[(\rho_v - \rho_l)\beta_l + \rho_l]} \tag{7}$$

$\beta_l$ is the liquid fraction and $M_{c.c}$ equals $M_{total} - M_{loop}$, and $M_{total}$ is the total mass of the working fluid which is filled by the operator. According to previous results [18, 19], the LHP gave the best performance for the liquid fraction ranging from 40% to 51.3 %.

The numerical scheme to calculate the vapor groove temperature and the energy balance equation is the Newton-Raphson method. A Fortran code and a thermal property program are used for computation.

To decide the outer diameter of the evaporator ($D_{e,o}$), a one-dimensional fin conduction model is applied [20]. The saddle and evaporator lengths are assumed to be the same as the length of the heat source, as shown in Fig. 3. And the saddle width is equal to the battery width.

$$\begin{aligned}
&Q_{u.s} = 2k_{eq}[\eta_{e,sad} B_{e,sad} + r_{cv,o}](T_{eq} - T_{so})L_e/(\delta_{eq}/2)\\
&Q_{u.s} = 2k_{e,sad}[\eta_{e,sad} B_{e,sad} + r_{cv,o}](T_{so} - T_{si})L_e/(\delta_{e,sad}/2)\\
&Where, \eta_{e,sad} = \tanh(m B_{e,sad})/(mB_{e,sad}),\\
&\quad m = \sqrt{G_{eq}/(k_{e,sad}\delta_{e,sad})},\ B_{e,sad} = W_{e,sad}/2 - r_{cv,o}\\
&Q_{load} = k_{cv,w}\pi D_{e,o}\eta_{cv,w}(T_{si} - T_{e,o})L_e/\delta_{cv,w}
\end{aligned} \tag{8}$$

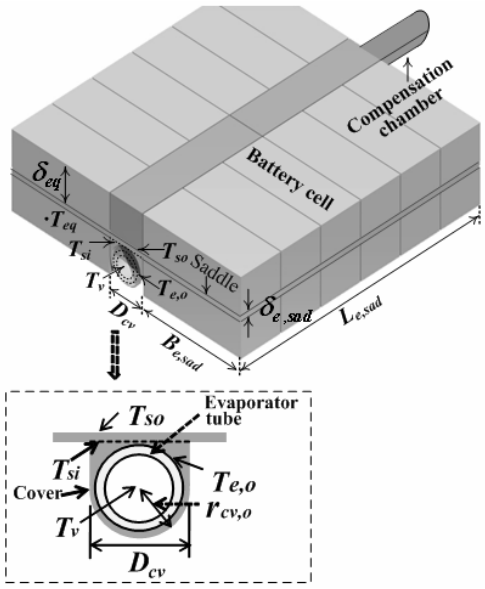


Fig. 3. Schematic of Battery pack (26 battery cells, Outer surface is insulated).

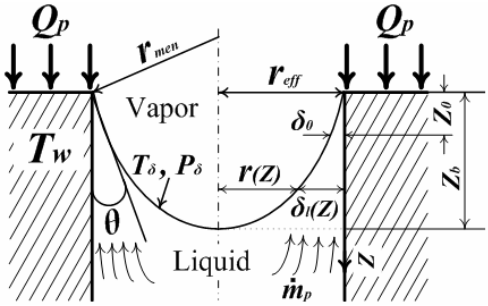


Fig. 4. Heat Transfer in the Pore of the Porous wick [5].

$$\begin{aligned}
&Where, \eta_{cv,w} = \tanh(P\pi D_{e,o}/2)/(P\pi D_{e,o}/2),\\
&\quad P = \sqrt{G_p/(k_{cv,w}\delta_{cv,w})},\ G_p = k_{e,w}/\delta_{e,w}\\
&Q_{load} = 2\pi k_{e,w}(T_{e,o} - T_{e,i})L_e/\log(D_{e,o}/D_{e,i})
\end{aligned}$$

$r_{cv}$ is the radius of the cover which surrounds the outer tube of the evaporator. In Eq. (8), $G_{eq}$ and $G_p$ are the thermal conductance per unit area of the interfaces. In this equation, $Q_{u.s}$ is the heat load generated from upper portion of the battery pack. Because the smallest surfaces of the batteries in low portion of the battery pack contact to the evaporator side, the temperature of the upper portion is higher than that of the lower portion. Therefore, it is sufficient to consider the temperature of the upper portion.

### *2.2 Heat transfer analysis of the porous wick*

In the pore of the porous wick of this study, the thin liquid film evaporation is assumed to be dominant. By the thin liquid film model [5], the evaporator wall temperature and the heat transfer coefficient depend on a sintered particle size, the porosity ( $\varepsilon$ ), et al. The heat transfer on the extended meniscus is shown in Fig. 4. In this paper, the wick is assumed to be well

saturated, and the total pressure drop should be less than the capillary force, as given by Eq. (9). $\Delta P_{loop}$ is the pressure drop excluding the drop in the evaporator.

$$\Delta P_{capillary} \geq \Delta P_{wick} + \Delta P_{loop} + \rho_l g \delta_{wick} \tag{9}$$

The wick pressure drop and the capillary pressure are calculated by Eq. (10), ( 11).

$$\Delta P_{wick} = \mu \dot{m} \ln(D_{wick,o} / D_{wick,i}) / (K 2\pi L_{wick} \rho) \tag{10}$$

$$\Delta P_{capillary} = 2\sigma Cos\theta / r_{eff} = 2\sigma / r_{men} \tag{11}$$

$K$ is permeability. In the evaporating thin film, a static contact angle ( $\theta$ ) is applied, because the dynamic contact angle is negligible [21]. The minimum contact angle relates a peak heat transfer coefficient [5] that is assumed to be 25°. The effective radius ( $r_{eff}$ ) is the same as 0.42 times the particle radius.

The local liquid film thickness ( $\delta_l$ ) is computed by using the effective and the meniscus radius ( $r_{men}$ ).

$$\delta_l(z) = r_{eff} - \sqrt{r_{men}^2 - \left(\sqrt{r_{men}^2 - r_{eff}^2} + z\right)^2} \tag{12}$$

To calculate $T_w$ , a temperature ( $T_\delta$ ) at the meniscus is computed by Wayer et al.'s evaporation heat flux model [22] and the pressure ( $P_\delta$ ) is acquired by the extended Kelvin equation. The disjoining pressure used to compute $P_\delta$ is given by the papers . [21, 23].

The temperature at the meniscus is given by Eq. (13).

$$T_\delta(z) = T_w + \frac{\delta_l(z)}{k_l}\left(\frac{2\alpha}{2-\alpha}\right)\frac{h_{fg}}{\sqrt{2\pi R_g}}\left[\frac{P_{sat}(T_v)}{\sqrt{T_v}} - \frac{P_\delta(z)}{\sqrt{T_\delta(z)}}\right] \tag{13}$$

The heat flow through a single pore using latent heat is expressed as $Q_{p1}$ and another heat flow ( $Q_{p2}$ ) equation is formulated by using the conduction equation.

$$Q_{p1} = [\dot{m} h_{fg} \pi r_{eff}^2] / \varepsilon$$

$$Q_{p2} = \int_{z_o}^{z_b} k_l \frac{T_w - T_\delta(z)}{\delta_l(z)} 2\pi r(z) dz \ ; \ r(z) = r_{eff} - \delta_l(z) \tag{14}$$

To calculate the heat transfer of the wick, (1) assume $T_w$ , then calculate $T_\delta$ ; (2) compare the heat flow ( $Q_{p1}$ ) with another heat flow ( $Q_{p2}$ ) obtained by Eq. (14). If they are not the same, $T_w$ is updated until satisfying equivalence. After the equivalence, the heat transfer coefficient is obtain by $H_{pre} = \dot{q} / (T_w - T_v)$ .

The critical heat load of the wick is given as follows.

$$Q_{b,\max} = \frac{2\pi L_e k_{eff} T_v}{h_{fg} \rho_v \ln(r_{wick,o} / r_{wick,i})}\left(\frac{2\sigma}{r_n} - P_{capillary}\right) = \frac{4\pi\sigma L_e k_{eff} T_v}{h_{fg} \rho_v \ln(r_{wick,o} / r_{wick,i})}\left(\frac{1}{r_n} - \frac{1}{r_{men}}\right) \tag{15}$$

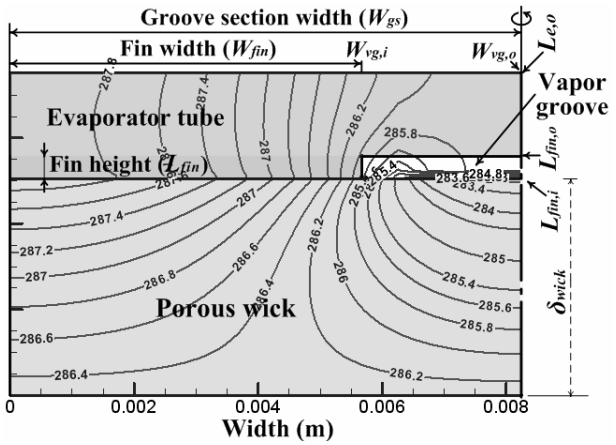


Fig. 5. Temperature distribution of groove section ( $T_{vg}$ : 286.3$K$, $q_{in}$ : 70$W$, $W_{gs}$ : 8.24, $W_{fin}$ : 5.84$mm$, $\varepsilon$ : 60% ).

$r_n$ is a nucleation radius and varies from 2.54x10$^{-8}$ to 2.54x10$^{-7}$ in the absence of noncondensable gases [24].

### *2.3 Heat transfer analysis of the groove section*

Fig. 5 shows the temperature distribution of the groove section. The average evaporator tube temperature and the evaporator mass are references for the optimization of the groove section.

$$k\frac{\partial^2 T}{\partial x^2} + k\frac{\partial^2 T}{\partial y^2} + \dot{q}/n_x = 0 \tag{16}$$

$$x = 0, \quad x = L_{e,o} : \ \frac{\partial T}{\partial x} = 0 \tag{17}$$

$$y = L_{fin,i} \ , \ and \ \ 0 \leq x \leq W_{fin} :$$

$$k\frac{\partial T}{\partial y} = -\dot{q}_{out} \cong \dot{q} - \dot{q}_{loss} \cong \dot{m} h_{fg} \tag{18}$$

$$y = L_{e,o} \ , and \ \ 0 \leq x \leq W_{fin} : \ \ k\frac{\partial T}{\partial y} = \dot{q} \tag{19}$$

$$W_{vg,i} \leq x \leq W_{vg,o} \ , \quad y = L_{fin,i} \ \ and \ \ y = L_{fin,o} :$$

$$k\frac{\partial T}{\partial y} = H_{vg}(T_{vg} - T_{fin,o}),$$

$$k\frac{\partial T}{\partial x} = H_{vg}(T_{vg} - T_{vg,i}) \tag{20}$$

A wider fin of the groove section is beneficial to the thermal performance, despite the mass increment. And the fin height is related to the sonic limit.

Cao et al's [6] analytical solution is adopted to acquire effects of the fin width. In this model, the two phase region is assumed to be very short and occurs at the contact area between the fin and the porous wick.

The conduction equation of the fin and the tube is given by Eq. (16). It is solved by FDM using the temperature distribution of the top wick surface calculated by analytical solution.

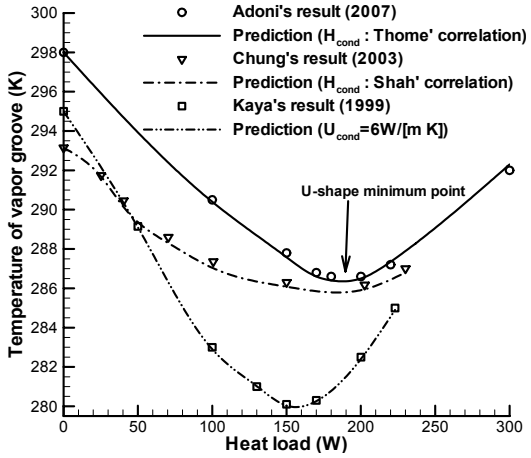


Fig. 6. Comparing present results with previous data.

This heat transfer problem is solved by the Cartesian coordinate equation, because the wick and the fin are thin. In Eq. (16) $\dot{q}$ is the heat flux on the outer evaporator surface and also the evaporation heat on the contact area. $H_{vg}$ is the forced convection heat transfer coefficient.

### *2.4 The validation of numerical computation*

Fig. 6 shows the validation results of computations.

The present studies are compared with the previous results of Adoni et al. [12], Chung [16] and Kaya [3]. The prediction for Adoni's result is computed by Thome's correlation [14].

In this figure, the evaporator temperature curve as a function of the heat load is U-shaped. U-shaped curves are most often observed for metal porous wicks, when ammonia is used as the working fluid and the temperature difference between the sink and the ambient is large [25].

## 3. Formulation of design problem

If the power of the laser system is 100kW and the efficiency is 15%, the required power is 650 kW. 450 kW is supplied by the battery and the remaining power is provided from the aircraft engines. In this case, the total number of the battery packs is 56 by the specific power of 1100W/kg at 5C.

One battery pack size is 24 (L) × 23 (W) × 6.4cm (H) and weighs 7.3kg. The pack consists of 26 battery cells, as shown in Fig. 3. Additionally, the heat generated from one battery pack from 60 to 110W makes the battery cell hotter than the ambient by about 35-64℃ (with $H_{amb} = 10 W m^{-2} K^{-1}$), when a cooling device is not equipped. If a storage temperature is about 10℃ (20℃), the permanent capacity loss is 10% (20%) of the total capacity after 1 year use [9].

Therefore, maintaining the temperature of the battery near 10℃ results in reduction of the maintenance cost and guarantee of high efficiency and reliability.

### *3.1 LHP using condition and configuration [Fig. 1, 3]*

The operating temperature of the Lithium Ion battery is set to be between 281.15K and desired value and a thermal conductivity of the battery is 3.4W/m K [26]. The aircraft is assumed to fly at 190~210 knots at altitudes of 26,000ft. The ambient temperature of the electronic room is 308K, and the outer air temperature is 243K. The total heat dissipation of one battery pack is from 60W to 110W. The evaporator length is the same as the battery pack length and the compensation chamber length is decided by the constraint condition using Eq. (7). Additionally, the inner diameter of the compensation chamber is set to be the same as the outer diameter of the evaporator. The evaporator saddle is 24 (L) x 23 (W) x 0.25cm (H). The saddle of the condenser is attached to the skin of the side fuselage and its thickness is 0.002m. The vapor and liquid line lengths are 1.0, 1.5 meters, respectively. The vapor line is sufficiently insulated. The tube thicknesses of the evaporator, the compensation chamber, the condenser and the transport line are 1.5, 1.5, 1 and 0.8mm, respectively. The wick thickness is 20% of the radius of the inner evaporator diameter because the thin wick is good to heat transfer and the weight reduction [4]. The working fluid is ammonia and the whole body is made of aluminum except the saddles and the wick, which are produced with magnesium and nickel, respectively.

Table 1. The design variables and ranges.

| Design variables | Design Space | | | Material |
|---|---|---|---|---|
| | Min | Base | Max | |
| Heat load (W) | 56 | 88 | 120 | . |
| $D_{e,o}$ (Cm) | 2.4 | 3.5 | 4.6 | Al |
| $D_{l.l,ins}$ (Cm) | 1 | 3 | 5 | Cork |
| $L_{cond}$ (m) | 0.8 | 1.15 | 1.5 | Al |
| $W_{c,sad}$ (cm) | 6.5 | 10.5 | 8.5 | Mg |
| $\varepsilon$ (%) | 40 | 50 | 60 | Ni |
| Ratio of $D_{prtl}$ (%) | 85 | 90 | 95 | Ni |
| $N_{vg}$ (EA) | 4 | 7 | 10 | Al |
| Ratio of $W_{fin}$ (%) | 33 | 50 | 77 | Al |
| Ratio of $L_{fin}$ (%) | 90 | 94 | 98 | Al |

Constraints

| | | |
|---|---|---|
| T (K) | Thermohydraulic model | Min: 281.15<br>Max: Desired |
| | Thin film<br>groove conduction | Pre-decided<br>temperatures |
| Mass (Kg) | Body+Fluid | Max: 2 kg |

### *3.2 Selection of design variables*

The design variables and space for the LHP optimization are summarized in Table 1. Here, the particle diameter ratio is the percentage of the applied particle diameter to the required particle diameter based on the capillary pressure limit. The fin width ($W_{fin}$) ratio indicates the percentage of the fin contact area to the groove section width. The fin length ($L_{fin}$) ratio is the proportion of the inner evaporator tube diameter to the outer porous wick diameter.

The diameter of the transport line predominantly affects the pressure drop and the mass of the LHP more than the temperature of the LHP. In this study, the inner transport line diameter is set to 2 mm, because the total pressure drop and gradient must be lower than the desired values, respectively [27]. The mass of the transport line does not greatly affect the total mass of the LHP, because the percentage of the transport line mass to the total mass is about 4%.

As for explaining the condenser tube diameter, the thermal conductance of the condenser predominantly depends on the saddle area more than this diameter size. The effective diameter of Thome and Fridel correlations [14, 15] is from 3.1 to 21.4mm. In addition, a diameter smaller than 3mm produces large total pressure drops. Therefore, the tube diameter is set to be 3.1mm [27].

### *3.3 Definition of design problem*

The optimization process is executed for three cases to reduce the mass of LHP as the battery temperature is maintained near 10℃.

Case I is the fixed heat load case in which the battery discharge rate is a fixed to a specific value.

Case II is the varied heat load case, in which the battery discharge rate is varied between 2C (60W) and 7C (110W) as the laser system power consumption rate. The optimized LHP for Case II must satisfy the temperature constraints, as the heat load is changed within a given range. The minimum temperature of the U-shaped curve should not be lower than the low battery temperature limit.

Case III is the varied heat load with uncertainty consideration case in which the uncertainty variable is the heat load of the battery. The uncertainty results from aging, fouling and position of the battery.

The optimization problem is defined as follows.

$$Find \quad x = \{x_1, x_2, x_3, x_4, x_5, \cdots\}^T \tag{21}$$

$$Minimize \quad F(x) = Mass_{LHP} \tag{22}$$

$$Subject \ \ to$$

$$x_i^L \le x_i \le x_i^U \quad for \ \ i = 1, n \tag{23}$$

$$\Delta P_{capillary,\,max} \ge \Delta P_{total}$$

$$Q_{load} \le Q_{boiling-limits}$$

$$Speed_{v.l/vg} \le 30\ \%\ of\ \ Speed\ of\ Sound$$

$$L_{c.c} \le Engineer\ description$$

Case I : Fixed Heat load

$$T_{low} \le T_{eq} \le T_{high} \quad for \ \ given \ \ Q_{load}$$

Case II : Varied Heat load

$$T_{low} \le T_{eq} \le T_{high} \quad for \ \ 60 \le Q_{load} \le 110W$$

$$T_{low} \le T_{U-s,min} \le T_{high} \quad for \ \ 60 \le Q_{load} \le 110W$$

Case III : Varied Heat load considering Uncertainty

$$Prob(T_{low} \le T_{eq} \le T_{high}) \ge 0.95 \quad for \ 60 \le Q_{avg} \le 110W$$

$$T_{low} \le T_{U-s,min} \le T_{high} \quad for \ \ 60 \le Q_{avg} \le 110W$$

$$\sigma_{heat\_load} = 4.5\%\ of\ Q_{avg} \quad for \ \ 60 \le Q_{avg} \le 110W$$

The low temperature limit is set to be 281.15K.

## 4. Design methodology

### *4.1 Building approximation model using RSM*

If analyses are accomplished, a quadratic response surface model is constructed as follows:

$$y^{(p)} = c_0 + \sum_i c_i x_i^{(p)} + \sum_{1 \le i \le j \le n_v} c_{ij} x_i^{(p)} x_j^{(p)} + \varepsilon, p = 1, \ldots, n_s \tag{24}$$

Where $y^{(p)}$ is the response; $x_i^{(p)}$ and $x_j^{(p)}$ are the $n_v$ design variables; and $c_0$, $c_i$ and $c_{ij}$ are unknown coefficients. More details are given by Kim [28]. The objective of using the RSM is to expedite the optimization process by reducing computation time.

As DOE (design-of experiment), the CCD (central composite design) and the modified CCD are applied. This will be explained in section 5.2 in detail.

### *4.2 Uncertainty consideration using Monte Carlo simulation as the reliability based method [29]*

The uncertainty variable is the heat generation of the battery cell; the heat generation has 4.5% standard deviation of the mean value and is assumed to be normally distributed. To compute probability of success, Monte Carlo simulation (MCS) is performed as the reliability based design optimization method. The number of samples for the MCS is 100,000. The constraint function ( $g(x)$ ) is transformed as follows.

$$Prob[g(Q_{avg})] = \int_{Q_{avg}-5\sigma}^{Q_{avg}+5\sigma} B[-g(Q)] J(Q)\, dQ \tag{25}$$

$B$ is the Heaviside step function and $J$ is probability density function, $Q$ is the uncertainty variable.

### *4.3 Optimization process*

The process of the optimization is shown in Fig. 7.

The optimization procedure is follows.

(1) Make the approximation models for the 3 analysis models using the RSM.

(2) Carry out the optimization using the themohydraulic approximation model.

(3) Optimize the porosity and the particle diameter of the wick with the outer wick diameter and the vapor groove temperature, etc. pre-decided in the thermohydraulic optimization section.

(4) Solve linked problem by iteration of the optimizer until the coupled design variable is converged. The coupled variable is the porosity.

(5) Optimize the groove section for the groove size.

(6) To consider the uncertainty, Optimizer II and III apply the max allowable heat load which is calculated by using the MCS in Optimizer I.

As optimization methods, SLP (sequential linear programming) and SQP (sequential quadratic program) methods are used.

Table 2. Effectiveness of optimization process.

| Component | Adoni's LHP | Optimized LHP |
|---|---|---|
| $D_{l1,i}$ (mm) | 4.57 | 3.05 |
| $D_{l1,ins}$ (cm) | 10 | 8.04 |
| $L_{cond}$ (m) | 3.00 | 3.02 |
| $D_{cond,i}$ (mm) | 4.57 | 4.48 |
| $T_{vg}$ (170/190/210$W$) | 287.4/287/287.4 | 287.4/287/287.4 |
| Mass (kg) | 2.74 | 2.41 |

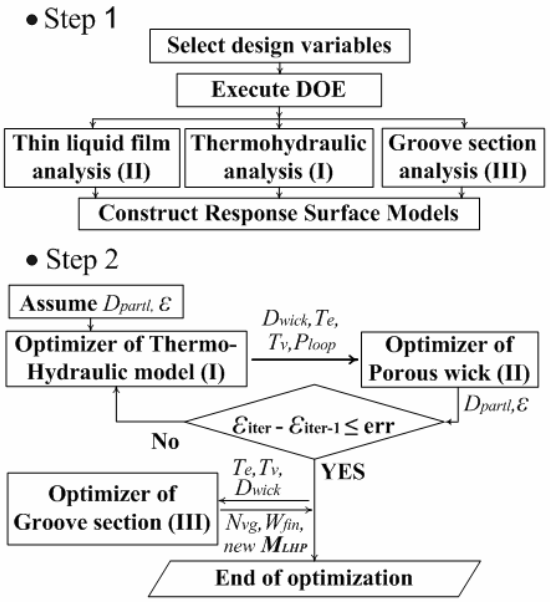


Fig. 7. Design procedure of the LHP using RSM.

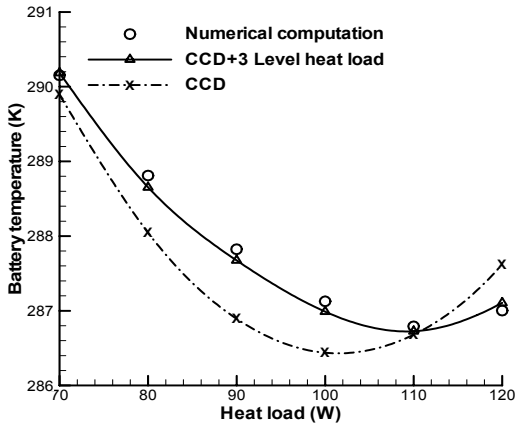


Fig. 8. Accuracy of Approximation model ( $D_e$ : 4.6, $D_{l1,ins}$ : 1, $W_{c,sad}$ : 8$cm$, $L_{cond}$ : 1.5$m$, $\varepsilon$ : 60% ).

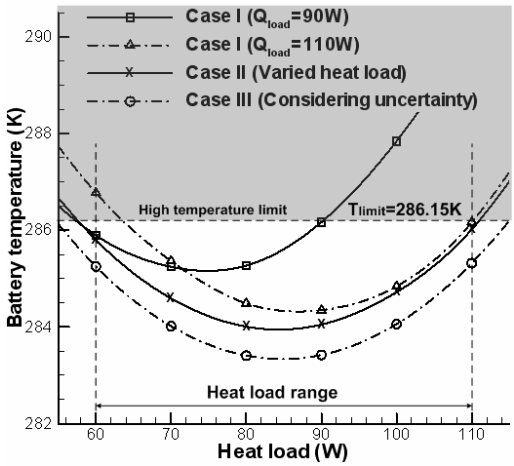


Fig. 9. Q-T curves of the optimized LHPs with respect to Case I, II, III.

## 5. Optimization result and discussion

### *5.1 Optimization effectiveness*

First, to verify usefulness of the optimization process, Adoni's LHP [12] is optimized with respect to 4 design variables as shown in Table 2.

To guarantee the same performance of the optimized LHP as that of previous LHP, 3 temperature constraints at 170, 190 and 210W are used. The total pressure drop should not be higher than the capillary force. The minimum contact angle is based on the reported hard-filled heat load. Total mass is reduced by 12 % compared with Adoni's LHP.

### *5.2 Accuracy of approximation model as DOEs*

The accuracy of the approximation models of the thermo-hydraulic analysis is checked in Fig. 8. The CCD+3 Level heat load DOE is executed to reflect the nonlinear features such as its characteristic U-shape curve. It uses 78 experiment points, because the 3 leveled heat loads (56,88,120W) are added to each experiment point which is constructed by the CCD and consists of 4 design variables. On the other hand, the CCD used 44 experimental points for the 5 design variables including the heat load variable.

The CCD+3 Level heat load DOE is more accurate than CCD. Therefore, the accuracy depends on the configuration of the experiment points.

In addition, the approximation models for the thin liquid film and the groove section analyses have about 99.6% accuracy as $R^2_{adj}$ value through applying the general CCD way.

### *5.3 Comparison of optimization results as cases*

Fig. 9 shows the Q-T curves of the optimized LHP for the three cases. The configurations of the four curves are described in Table 3. The temperatures of Case I for 90 watts and 110 watts violate the temperature constraints at 110 and 60 watts, respectively. Especially, it is important that the optimized LHP for the high heat load (110W) including a proper heat load margin could violate the temperature constraint at the low heat load (60W).

The curve of Case II satisfies the temperature constraints at 60W and 110W. As the temperature curve positions near the constraint at 110W, small heat load fluctuation causes the battery temperature to violate the unfeasible region. And the

Table 3. Optimization results of LHP.

| $T_{limit}$ =286.15K | Case I | | Case II | Case III |
|---|---|---|---|---|
| | $Q_{load}$ = 90W | $Q_{load}$ = 110W | $60W \le Q_{load} \le 110W$ | Considering Uncertainty |
| $D_{e,o}$ (cm) | 2.404 | 2.966 | 3.073 | 3.112 |
| $D_{l,l,ins}$ (cm) | 4.923 | 4.195 | 4.628 | 4.192 |
| $L_{cond}$ (m) | **0.889** | **1.066** | **1.094** | **1.109** |
| $W_{c,sad}$ (cm) | 10.48 | 10.396 | 9.712 | 10.328 |
| $N_{vg}$ | **7** | 7 | 8 | 8 |
| $D_{prtl}$ (mm) | 0.379 | 0.056 | 0.059 | 0.042 |
| $W_{fin}$ (mm) | 3.165 | 4.229 | 3.697 | 3.859 |
| $L_{fin}$ (mm) | 0.403 | 0.856 | 0.811 | 0.808 |
| Success Ratio | 0.492 | 0.412 | 0.740 | 0.95 |
| $M_{LHP}$ (kg) | **1.277** | **1.482** | **1.517** | **1.549** |
| Characteristics | **Constraint violation at 60 or 110W** | | **Flexibility to heat load change** | **Reliability enhancement** |

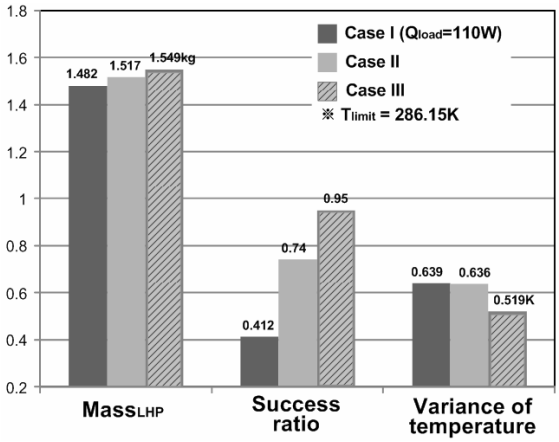


Fig. 10. Variation of mass, success ratio and variance.

gradient of the temperature curve for Case II is slacker than that of Case I for the 110W.

The battery temperature curve of Case III is much lower than the line of the constrained temperature limits, because the curve is computed by considering the normally distributed uncertainty of the heat load. Therefore, the optimized LHP of Case III has few possibilities of violating the temperature constraints.

Fig. 10 shows the variations of the mass, success ratio and a variance of the battery temperature for three cases depicted in Table 3. The success ratio indicates the proportion of experiment trials that satisfied the constraints to the total number of trials. And the success ratios and temperature variances of Case I, II are computed with the same heat load variance as that of Case III. The LHP of Case III is heavier than that of Case II by only 2.1%, but the success ratio is increased by 28% and the battery temperature variance is enhanced by 18% compared with Case II. Therefore, the optimized LHP of Case III is considered to be robust to the uncertainty of the heat load with only small mass increment.

Table 3 shows the size of the optimized LHP and the success ratio in terms of the cases. The sintered particle diameter ($D_{prtl}$) of Case II is calculated at the heat load of 110W, because the largest pressure drop occurs at the heat load.

The optimized LHP of Case II consists of a relatively longer condenser than that of Case I. The LHP with the long condenser is characterized by a slack gradient of the temperature versus heat load curves [2]. Therefore, to satisfy the temperature limits in the broad range of the heat load, the longer condenser should be used for the varied heat load case.

The LHP of Case III has the longest condenser, because this case should endure heat load fluctuation ranging from approximately 53 to 116 watts.

In addition, the porosity is determined as the high boundary values of this variable by the optimization process, because the larger porosity yields a higher permeability and the higher permeability is beneficial to heat transfer enhancement [23] and mass reduction. But, the large porosity relates to the physical weakness. Therefore, deciding the proper porosity is performed in terms of the structural analysis.

## 6. Conclusions

In this work, the design optimization of the LHP was successfully performed for the fixed and the varied heat load cases to reduce the mass of the LHP with sustaining the battery temperature near 10℃. The high altitude cold air out of the aircraft, instead of artificial cooling, is used for condensation.

For the detailed optimization results for the porous wick and the groove section, the thin liquid film and the groove section analysis models are applied in addition to the thermohydraulic model.

Based on the optimization results, the mass of the LHP is reduced by 12% from that of Adoni' LHP under the same thermal conditions. The optimized LHP of the fixed heat load case could not satisfy the temperature constraints at the low heat load, although the LHP is designed for the high heat load.

The LHP of the varied heat load case could endure the heat load change by the mission requirement.

The varied heat load with uncertainty consideration case shows the best performance in terms of the success ratio and the variance of the battery temperature, despite only 2.1% mass increment. The condenser length of the case is longest among those of the three cases and affects strongly the battery temperature.

In general, the flying environment of the military aircraft requires rapid power changes and high robustness of the battery. Therefore, the varied heat load with uncertainty consideration case can be a good candidate for the LHP design for military uses.

## Nomenclature

$f$ : Darcy friction factor
$h_{fg}$ : Latent heat ( $J \cdot kg^{-1}$ )
$k$ : Thermal conductivity ($W \cdot m^{-1} \cdot K^{-1}$)
$M$ : Mass (kg)
$\dot{m}$ : Mass flow rate ( $kg \cdot s^{-1}$ )
$Q$ : Heat load (W)
$\dot{q}$ : Heat flux ( $W\ m^{-2}$ )
$R_g$ : Gas constant ( $J \cdot Kg^{-1} \cdot K^{-1}$ )
$U$ : Specific thermal conductance ( $W \cdot m^{-1} \cdot K^{-1}$ )
$W$ : Watts / width (m)
$x$ : Dryness fraction of vapor
$\delta$ : Thickness (m)
$\sigma$ : Surface tension ( $N \cdot m^{-1}$ ) / standard deviation

### *Subscripts*

*c.c* : Compensation chamber
*cond* : Condenser
*e* : Evaporator
*ins* : Insulator
*l.l* : Liquid line
*prtl* : Particle
*sat* : Saturation
*sad* : Saddle
*sink* : Air condition out of aircraft
*vg* : Vapor groove
*v.l* : Vapor line

## Acknowledgment

This work was supported by the second stage of BK21 (Brain Korea-21) School for Creative Engineering Design of Next Generation Mechanical and Aerospace Systems at Seoul National University of the Korean Ministry of Education, Science and Technology.

## References

[1] V. V. Vlassov, F. L. Sousa and R. R. Riehl, Design optimization of loop heat pipes with cylindrical evaporator and integral reservoir for space application, Space Technology and Applications international Forum-STAIF, (2008).

[2] Y. J. Park, J. Kim, S. Jun, M. Kwak and D. H. Lee, Multi-objective design optimization of loop heat pipe, 12th AIAA/ISSMO Multidisciplinary Analysis and Optimization Conference, 10-12 September, (2008), Victoria British Columbia Canada.

[3] T. Kaya and T. T. Hoang, Mathematical modeling of loop heat pipes and experimental validation, J. Thermophysics and Heat Transfer, 13 (3) (1999) 314-320.

[4] M. A. Hanlon and H. B. Ma, Evaporation heat transfer in sintered porous media, J. Heat Transfer, 125 (2003) 644-652.

[5] T. S. Zhao and Q. Liao, On capillary-driven flow and phase-change heat transfer in a porous structure heated by a finned surface: measurements and modeling, Intl. J. Heat and Mass Transfer, 43 (2000) 1141-1155.

[6] Y. Cao and A. Faghri, Analytical solutions of flow and heat transfer in a porous structure with partial heating and evaporation on the upper surface, Intl. J. Heat Mass Transfer, 37 (10) (1994) 1525-1533.

[7] J. P. Fellner and R. M. Miller, V. Shanmugasundaram, Rechargeable lithium ion based batteries and thermal management for airborne high energy electric lasers, SAE International, (2006), 1-8.

[8] S. A. Hallaj, H. Maleki, J. S. Hong and J. R. Selman, Thermal modeling and design considerations of lithium-ion batteries, J. Power Sources, 83 (1999) 1-8.

[9] I. Buchmann (September 2006). Battery university.com: How to prolong lithium-based batteries, Cadex Electronics Inc.

[10] M. Keyser, A. Pesaran, S. Oweis and G. Chagnon, Thermal evaluation and performance of high-power lithium-ion cells, the 16th Electric Vehicle Conference, October 1-3, (1999) Beijing, China.

[11] K. H. Token and R. S. Cook, Heat pipe avionic cooling, Proceedings of the national aerospace and electronics conference, Dayton, May, (1980).

[12] A. A. Adoni and A. Ambirajan, Thermohydraulic modeling of Capillary Pumped Loop and Loop Heat Pipe, J. Thermophysics and Heat Transfer, 21 (2) (2007) 410-421.

[13] Y. J. Kim and C. N. Kim, A numerical prediction and flight test of the transient fuel temperatures in an aircraft, J. Mechanical Science and Technology, 21 (2007) 2250-2260.

[14] M. R. Thome, J. E. Hajal and A. Cavallini, Condensation in horizontal tubes, part 2: new heat transfer model based on flow regimes, Intl. J. Heat Mass Transfer, 46 (2003) 3365-3387.

[15] L. Fridel, Improved friction pressure drop correlations for horizontal and vertical two-phase pipe flow, European Two-Phase Flow Group Meeting, Ispra, Italy, (1979) E241-1155.

[16] P.-Y. A. Chung, An improved steady-state model of loop heat pipes based on experimental and theoretical analysis, Ph.D. Dissertation, Dept. of Mechanical and Nuclear Eng, The Pennsylvania State University, PA, ( 2003).

[17] J. Ku, Operating characteristics of Loop Heat Pipes, SAE International 1999-01-2007, (1999).

[18] J. H. Boo and W. B. Chung, Experimental study on the

thermal performance of a small-scale Loop Heat Pipe with polypropylene wick, J of Mechanical Science and Technology, 19 (4) (2005) 1052-1061.
[19] W. H. Lee, K. W. Lee, K. H. Park and K. J. Lee, Study on working characteristics of loop heat pipe using a sintered metal wick, in; 13th IHPC, Shanghai, China, 21-25 Sept', (2004).
[20] V. V. Vlassov, F. L. Sousa and W. K. Takahashi, Comprehensive optimization of a heat pipe radiator assembly filled with ammonia or acetone, Intl. J. Heat Mass Transfer, 49, (2006), 4584-4595.
[21] K. P. Hallinan and H. C. Chebaro, Evaporation from an extended meniscus for non-isothermal interfacial conditions, J. Thermophysics and Heat Transfer, 8 (4) (1994) 709-716.
[22] V. P. Carey, Liquid-vapor phase-change phenomena: An introduction to the Thermophysics of vaporization and condensation processes in heat transfer equipment, Washington, DC, Taylor & Francis Series, Hemisphere Pub. Corp, (1992).
[23] D. Khrustalev and A. Faghri, Heat transfer in the inverted meniscus type evaporator at high heat fluxes,," Intl. J. Heat Mass Transfer. 38 (16) (1995) 3091-3101.
[24] S. W. Chi, Heat Pipe Theory and Practice, A Source book, Hemisphere Publishing Corporation, New York, (1976).
[25] S. Launay, V. Sartre and J. Bonjour, Analytical model for characterization of Loop Heat Pipes, J. Thermophysics and Heat Transfer, 22 (4) (2008) 623-631.
[26] H. Maleki, S. A. Hallaj, J. R. Selman, R. B. Dinwiddie and H. Wang, Thermal properties of lithium-ion battery and components, J. the Electrochemical Society, 146 (3), (1999), 947-954.
[27] Y. J Park, S. Yun, Y. Ku and D. H. Lee, Design optimization for loop heat pipe using tabu search, J. the Korean Society Aeronautical and Space Sciences, 37 (8) (2009) 737-743.
[28] Y. Kim, J. Kim, Y. Jeon, J. Bang, D. H. Lee and Y. Kim, Multidisciplinary aerodynamic-structural design optimization of supersonic fighter wing using response surface methodology, (2002), AIAA-2002-0322.
[29] C. Kim, S. Wang, K. Bae and Moon, Reliability-based topology optimization with uncertainties, J. Mechanical Science and Technology, 20 (4) (2006) 494-504.

**YongJin Park** has been a Ph.D candidate of Seoul National University since 03/ 2006 and received a Master's degree in 2001 at Yonsei University. The research topic of interest is a reliability based design optimization of a thermal system and a multi-criteria decision making.

**Sangook Jun** has been a Ph.D candidate (The integrated MA/Ph.D Course) since 03/ 2008 and received a Bachelor's degree in 2002 at Seoul National University. The research topic of interest is a robust design optimization and a reduced order model.

**Sanghun Kim** has been a Ph.D candidate since 03/ 2004 and received a Master's degree in 2004 at Seoul National University. The research topic of interest is a reliability design optimization of a helicopter.

**Dongho Lee** is a professor of Seoul National University and a member of The National Academy of Engineering of Korea. He was a director of IAAT (Institute of Advanced Aerospace Technology). He is interested in Computational Fluid Dynamics, wind tunnel test and Multidisciplinary Design Optimization for large and complex systems (e.g. aircraft, helicopter, high speed train, compressor and wind turbine).